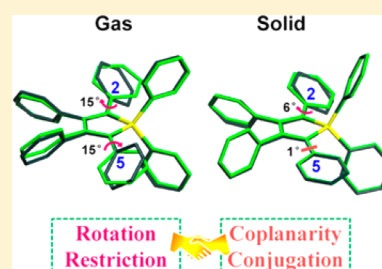


Aggregation Effects on the Optical Emission of 1,1,2,3,4,5-Hexaphenylsilole (HPS): A QM/MM Study

Tian Zhang,[†] Yuqian Jiang,[†] Yingli Niu,[‡] Dong Wang,[†] Qian Peng,^{*,‡} and Zhigang Shuai^{*,†}[†]Key Laboratory of Organic OptoElectronics and Molecular Engineering, Department of Chemistry, Tsinghua University, Beijing 100084, P. R. China[‡]Key Laboratory of Organic Solids, Beijing National Laboratory for Molecular Science (BNLMS), Institute of Chemistry, Chinese Academy of Sciences, Beijing 100190, P. R. China

S Supporting Information

ABSTRACT: We investigate the photophysical property for 1,1,2,3,4,5-hexaphenylsilole (HPS) through combined quantum mechanical and molecular mechanical (QM/MM) simulations. Under the displaced harmonic oscillator approximation with consideration of the Duschinsky rotation effect (DRE), the radiative and nonradiative rates of the excited-state decay processes for HPS are calculated by using the analytical vibration correlation function approach coupled with first-principles calculations. The intermolecular packing effect is incorporated through electrostatic interaction modeled by a force field. We find that from the gas phase to the solid state (i) the side phenyl ring at the 5-position becomes coplanar with the central silacycle, which increases the degree of conjugation, thus accelerating the radiative decay process, and (ii) the rotation of the side phenyl ring at the 2-position is restricted, which blocks the excited-state nonradiative decay channels. Such a synergetic effect largely enhances the solid-state luminescence quantum efficiency through reducing the nonradiative decay rate by about 4 orders of magnitude, leading to the radiative decay overwhelming the nonradiative decay. In addition, the calculated solid-phase absorption and emission optical spectra of HPS are found to be in agreement with the experiment.



I. INTRODUCTION

Efficient solid-state light-emitting materials have attracted great attention for thin film display and lighting technology.^{1–3} Aggregation-caused quenching (ACQ) or concentration quenching in many molecular systems due to the intermolecular charge or energy transfer, formation of nonemissive or low-emissive “side-by-side” H-aggregates or detrimental species such as excimers, has been considered as an obstacle toward high-performance optoelectronic devices.^{4–6} Both chemical and physical approaches have been employed to conquer the ACQ effect but with difficulties.^{7–11} The aggregation-induced emission (AIE) phenomenon proposed and systematically explored by Tang et al. provides a straightforward and effective way to solve the ACQ problem.^{12,13} AIE-active molecules are nonemissive or low emissive in dilute solution but become strongly emissive in the aggregate state. To figure out the molecular luminescent mechanism in aggregates, well-defined single crystals seemed to be interesting in revealing the intrinsic nature of intermolecular interaction and identifying the structural factors that force the molecules into a particular conformation. Oelkrug et al. have noted that solid-state packing can suppress nonradiative torsional deactivation in electron-withdrawing-group-substituted oligophenylenevinylene derivatives.¹⁴ Gierschner and Park have systematically analyzed the relationships between the single crystal structures and solid-state optical properties of a series of functionalized distyrylbenzene (DSB), and they stress that the cyanovinylene motif shows an AIE enhancement (AIEE) behavior due to both

twist elasticity and secondary bonding interaction.¹⁵ Nevertheless, the range of order for the molecular solid is typically short due to weak intermolecular interaction. In most cases, the solid phase is not a single crystal. It is important to explore the excited-state property for general molecular aggregates. In this respect, the exciton–phonon model has been extensively employed for understanding the optical spectral characteristics for conjugated polymers and oligomers.¹⁶

Various AIE mechanisms have been proposed experimentally, including restriction of intramolecular rotation (RIR),^{4,17} coplanarization,¹⁸ J-aggregates formation,¹⁹ excimer formation,²⁰ etc. We have interpreted the AIE phenomena through elucidating the excited-state decay vibronic couplings. It was pointed out that the low-frequency vibrational modes are easily mixed each other upon electronic excitation; namely, the Duschinsky rotation effect (DRE) plays an important role in describing the excited-state nonradiative decay rates.^{21–25} Hayashi et al. investigated the internal conversion (IC) process of solid-phase diphenyl dibenzofulvene (DPDBF) based on the ONIOM method.²⁶ We investigated the aggregation effects on the excited-state decays of the AIE-active molecules by using a

Special Issue: International Conference on Theoretical and High Performance Computational Chemistry Symposium

Received: February 28, 2014

Revised: June 12, 2014

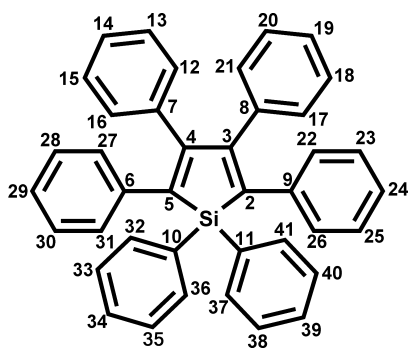
Published: June 12, 2014



quantum mechanics and molecular mechanics (QM/MM) approach coupled with thermal vibration correlation function (TVCF) formalism.^{27,28} Recently we employed nonadiabatic surface hopping dynamics to explore the excited-state non-radiative decay processes for “open” and “closed” DPDBF.²⁹ Through high-level *ab initio* quantum-chemical (MS-CASPT2//CASSCF) calculations, Li et al. pointed out that the conical intersection (CI) seam occurring in acetonitrile solution cannot be accessed in aggregates, and therefore DPDBF becomes emissive in the molecular solid.³⁰

Siloles (silacyclopentadines) were the first AIE-active luminogens exhibiting both high charge carrier mobility and photoluminescence (PL) efficiency in condensed phase.^{5,13,21,31} The 1,1,2,3,4,5-hexaphenylsilole (HPS) is poorly luminescent in cyclohexane at room temperature, with a fluorescence quantum yield (Φ_F) as low as 0.30%. However, the emission efficiency in the thin film phase increases to 78%, namely a 260-fold increase.^{4,21} The primary purpose of this work is to investigate the aggregation emission behaviors of the representative member of the silole family, HPS (Chart 1),

Chart 1. Chemical Structure of HPS



from computational elucidation. The methodologies have been successfully applied to rationalize the AIE phenomena of *cis,cis*-1,2,3,4-tetraphenyl-1,3-butadiene (TPBD),²³ 9-[(*o*-aminophenyl)phenylmethylene]-9*H*-fluorene (APPEF),²⁴ 2,3-dicyano-5,6-diphenylpyrazine (DCDPP),^{25,27} and 3-(2-cyano-2-phenylethenyl-*Z*)-NH-indole (CPEI).^{28,32} For the sake of simplicity, we model HPS in the gas phase without considering the solvent polarity because the photophysical properties were measured in the nonpolar cyclohexane dilute solution.

II. METHODOLOGY

Radiative decay rate (k_r) and nonradiative decay rate ($k_{nr} = k_{IC} + k_{ISC}$) are important parameters for the excited-state decay processes, where k_{IC} and k_{ISC} are nonradiative IC and intersystem crossing (ISC) rate, respectively. In most organic molecules, k_{ISC} can be neglected owing to the small spin-orbital coupling (SOC) for the $\pi \rightarrow \pi^*$ electron transition.²⁴ Electron excited-state dynamics, such as the Ehrenfest^{33,34} and surface hopping dynamics,^{35–37} has been successfully applied to investigate the nonadiabatic electron dynamics or to treat the CIs. However, the decay rate of CI is usually greater than 10^{12} s^{-1} , much faster than the typical radiative decay rates in OLEDs of approximately 10^7 – 10^8 s^{-1} .^{27,28} For complex polyatomic molecule, nuclear-motion degrees of freedom could be reasonably assumed to be close to the equilibrium position upon photoexcitation.³⁸ In this contribution, based on the Fermi Golden Rule (FGR), we adopt a multidimensional mixed

harmonic oscillator model and a TVCF formalism to describe both the radiative and nonradiative processes.

A. Absorption and Emission Spectra. The absorption $\sigma_{ab}(\omega, T)$ and emission $\sigma_{em}(\omega, T)$ spectra are expressed as follows:

$$\sigma_{ab}(\omega, T) = \frac{4\pi^2\omega}{3\hbar c} \sum_{u,\nu} P_{i\nu} |\langle \Theta_{i\nu} | \mu_{fi} | \Theta_{iu} \rangle|^2 \delta(\omega - \omega_{iu, i\nu}) \quad (1)$$

$$\sigma_{em}(\omega, T) = \frac{4\omega^3}{3\hbar c^3} \sum_{u,\nu} P_{i\nu} |\langle \Theta_{i\nu} | \mu_{fi} | \Theta_{iu} \rangle|^2 \delta(\omega_{iu, i\nu} - \omega) \quad (2)$$

$P_{i\nu}$ is the initial-state Boltzmann distribution function for the vibronic manifold at finite temperature. Θ is the nuclear vibrational wave function. ν and u are vibrational quantum numbers. μ_{fi} is the electric transition dipole moment between the two electronic states $|\Phi_i\rangle$ and $|\Phi_f\rangle$, which does not depend on nuclear coordinate under the Franck–Condon approximation. Fourier transforming the delta function in eqs 1 and 2 gives the analytical integral formalisms:

$$\sigma_{ab}^{FC}(\omega, T) = \frac{2\pi\omega}{3\hbar c} |\mu_0|^2 \int_{-\infty}^{\infty} e^{i(\omega - \omega_{if})t} Z_i^{-1} \rho_{ab,0}^{FC}(t, T) dt \quad (3)$$

$$\sigma_{em}^{FC}(\omega, T) = \frac{2\omega^3}{3\pi\hbar c^3} |\mu_0|^2 \int_{-\infty}^{\infty} e^{-i(\omega - \omega_{if})t} Z_i^{-1} \rho_{em,0}^{FC}(t, T) dt \quad (4)$$

where Z_i is the partition function and the correlation functions $\rho_{ab,0}^{FC}(t, T)$ and $\rho_{em,0}^{FC}(t, T)$ can be written as

$$\rho_{ab,0}^{FC}(t, T) = \rho_{em,0}^{FC}(t, T) = \text{Tr}[e^{-i\tau_f \hat{H}_f} e^{-i\tau_i \hat{H}_i}] \quad (5)$$

$\tau_i = -i\beta - t/\hbar$, $\tau_f = t/\hbar$, $\beta = (k_B T)^{-1}$, and k_B is the Boltzmann constant. \hat{H}_f and \hat{H}_i are the multidimensional harmonic-oscillator Hamiltonians for the final and initial electronic states, respectively. Analytical solution to eq 5 can be obtained by virtue of Gaussian integration.³⁹

B. Radiative Decay and Nonradiative IC Rates. The general radiative decay rate equation for polyatomic systems can be obtained by integration over the whole emission spectrum:

$$k_r(T) = \int \sigma_{em}(\omega, T) d\omega \quad (6)$$

With FGR, the IC rate can be expressed as

$$k_{ic} = \frac{2\pi}{\hbar} |H'_{fi}|^2 \delta(E_{fi} + E_{fu} - E_{iv}) \quad (7)$$

where the perturbation H'_{fi} is the non-Born–Oppenheimer coupling:

$$H'_{fi} = -\hbar^2 \sum_l \left\langle \Phi_f | \Theta_{fi} \left| \frac{\partial \Phi_i}{\partial Q_{fl}} \frac{\partial \Theta_{iv}}{\partial Q_{fl}} \right. \right\rangle \quad (8)$$

Under the Condon approximation, eq 8 becomes

$$H'_{fi} = \sum_l \langle \Phi_f | \hat{P}_{fl} | \Phi_i \rangle \langle \Theta_{fu} | \hat{P}_{fl} | \Theta_{iv} \rangle \quad (9)$$

where $\hat{P}_{fl} = -i\hbar \partial / \partial Q_{fl}$ is the normal mode momentum operator.

When eq 9 is inserted into eq 7, the IC rate can be written as

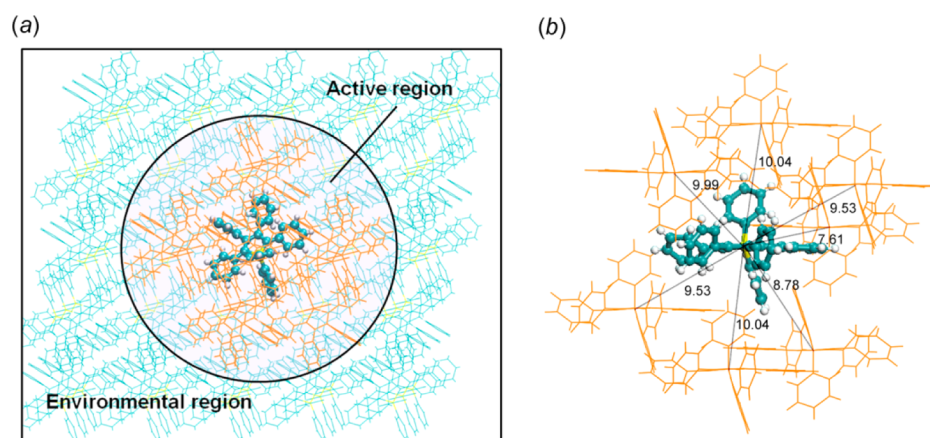


Figure 1. (a) QM/MM model: single centered HPS molecule is treated quantum mechanically for the electronic excited state; its 11 nearest molecules are optimized at the MM level; and the remaining 63 molecules are fixed at the MM level as environment. (b) Close look at the packing structure with intermolecular distances labeled in Å.

$$k_{\text{IC}} = \sum_{kl} k_{\text{ic},kl} \quad (10)$$

$$k_{\text{ic},kl} = \frac{2\pi}{\hbar} R_{kl} Z_i^{-1} \sum_{v,u} e^{-\beta E_{iv}} P_{kl} \delta(E_{fi} + E_{fu} - E_{iv}) \quad (11)$$

where

$$R_{kl} = \langle \Phi_i | \hat{P}_{fk} | \Phi_i \rangle \langle \Phi_i | \hat{P}_{il} | \Phi_i \rangle \quad (12)$$

$$P_{kl} = \langle \Theta_{fu} | \hat{P}_{ik} | \Theta_{fu} \rangle \langle \Theta_{iv} | \hat{P}_{il} | \Theta_{iv} \rangle \quad (13)$$

Fourier transforming the delta function of eq 11, we obtain

$$k_{\text{ic},kl} = \frac{1}{\hbar^2} R_{kl} \int_{-\infty}^{\infty} dt [e^{i\omega_{iv}t} Z_i^{-1} \rho_{\text{ic},kl}(t, T)] \quad (14)$$

where $\rho_{\text{ic},kl}(t, T)$ is the TVCF in the IC process,

$$\rho_{\text{ic},kl}(t, T) = \text{Tr}(\hat{P}_{fk} e^{-i\tau_i \hat{H}_i} \hat{P}_{il} e^{-i\tau_f \hat{H}_i}) \quad (15)$$

More details of IC correlation function can be found in our previous work.^{39,40}

The vibration-mode mixing effect can be taken into accounts as $Q_{ik} = \sum_l^{3n-6} \mathbf{S}_{kl} Q_{il} + \mathbf{D}_k$, where \mathbf{S} is the Duschinsky rotation matrix (DRM) representing the mixing of normal modes in the initial and final states and the vector \mathbf{D}_k is the displacement along the normal mode k between the minima of the ground and excited-state geometries. \mathbf{S}_{kl} and \mathbf{D}_k are calculated following Reimers' algorithm.^{39,41}

First-order perturbation theory is applied to compute the electronic coupling R_{kl} following Lin.⁴² Expressing the electronic coupling term at the equilibrium position approximately, we get

$$\langle \Phi_i | \hat{P}_{il} | \Phi_i \rangle = -i\hbar \langle \Phi_i | \frac{\partial}{\partial Q_{il}} | \Phi_i \rangle = -i\hbar \frac{\langle \Phi_i^0 | \partial \hat{U} / \partial Q_{il} | \Phi_i^0 \rangle}{E_i^0 - E_f^0} \quad (16)$$

where

$$\langle \Phi_i^0 | \partial \hat{U} / \partial Q_{il} | \Phi_i^0 \rangle = - \sum_{\sigma} \frac{Z_{\sigma} e^2}{\sqrt{M_{\sigma}}} \sum_{\tau=x,y,z} E_{f \leftarrow i, \sigma \tau} L_{\sigma \tau, l} \quad (17)$$

the transition electric field $E_{f \leftarrow i, \sigma \tau} = \int d\mathbf{r} \rho_{if}^0(\mathbf{r}) \mathbf{e}(r_{\tau} - R_{\sigma \tau}) / |\mathbf{r} - \mathbf{R}_{\sigma}|^3$ can be computed directly from TD-DFT calculation, and U is the electron–nuclear potential term in the Hamiltonian.

C. Computational Approach. The excited-state calculation is carried out by TD-DFT for single molecule, and the aggregation effect is modeled by QM/MM approach. The solid-phase computational model for HPS was set up on the basis of the X-ray crystal structure. The computational model consists of 75 molecules (5325 atoms) where one central molecule (71 atoms) is defined as the QM region. During the QM/MM geometry optimizations, the active region (defined as a sphere with a radius of 12 Å surrounding the QM centroid) was allowed to move, whereas all the remaining molecules were kept fixed as the environment (Figure 1a). A close look at the intermolecular packing structure is shown in Figure 1b. The QM/MM calculations were carried out using the ChemShell 3.5 package⁴³ integrating Turbomole 6.5^{44,45} (QM part) with DL-POLY⁴⁶ (MM part) programs. The general Amber force field (GAFF) was used for the MM treatment.⁴⁷ Because the parameters for silicon is not available in GAFF, for the bonded part we used the same force constants as the sp^3 -hybridized carbon, while leaving the equilibrium structural parameters consistent with those of the crystal structure; for the nonbonded part, Lennard-Jones parameters were inherited from Dock package, assigning 2.220 Å for the radius and 0.320 kcal/mol for the well depth.⁴⁸ The restrained electrostatic potential (RESP) approach at HF/6-31G* level was used to assign partial charges.^{49,50} The electrostatic embedding scheme was adopted in the QM/MM treatment.⁵¹

The equilibrium geometries were determined at the DFT/TD-DFT level. No symmetry constraint was adopted for both gas- and solid-phase optimizations. The B3LYP functional^{52,53} was used with the 6-31G* basis set.⁶ The analytical frequencies of S_0 at the DFT level and numerical frequencies of S_1 at the TD-DFT level have been evaluated, and the absence of imaginary frequencies in the gas phase was carefully checked. The solid-phase frequencies were obtained by using the numerical differentiation method, including the electronic polarization effect from the environments. The transition atomic electric field appeared in the electronic coupling term was calculated using the D.01 version of the Gaussian 09 package.⁵⁴ Here, it should be mentioned that several approximations were made: (i) we do not consider intermolecular charge transfer, energy transfer, or exciton effect; (ii) the charge distribution of the surrounding molecules re-equilibrating with the QM electron density in the excited state is not taken into account as limited by GAFF. To address

Table 1. Selected Bond Lengths (Å), Bond Angles (deg), and Dihedral Angles (deg) of Gas-Phase and Solid-Phase HPS at the S_0 (S_1) Minimum

	gas phase			solid phase			crystal ^a
	S_0	S_1	$ \Delta(S_0-S_1) $	S_0	S_1	$ \Delta(S_0-S_1) $	
Si–C2	1.8894	1.8736	0.0158	1.8850	1.8673	0.0177	1.8617
Si–C5	1.8893	1.8738	0.0155	1.8982	1.8831	0.0151	1.8742
Si–C10	1.8888	1.9014	0.0126	1.9004	1.9120	0.0116	1.8744
Si–C11	1.8888	1.9014	0.0126	1.8952	1.9051	0.0099	1.8646
C2–C9	1.4795	1.4507	0.0288	1.4769	1.4463	0.0306	1.4804
C5–C6	1.4796	1.4510	0.0286	1.4802	1.4528	0.0274	1.4789
C3–C8	1.4929	1.4792	0.0137	1.4950	1.4808	0.0142	1.4877
C4–C7	1.4929	1.4793	0.0136	1.4970	1.4946	0.0024	1.4943
Si–C2–C3	107.32	109.22	1.90	107.00	108.64	1.64	107.15
C2–C3–C4	116.36	115.31	1.05	116.39	115.29	1.10	116.05
C2–Si–C5	92.52	90.90	1.62	93.11	91.61	1.50	93.20
C10–Si–C11	111.45	108.40	3.05	112.63	110.39	2.24	111.65
Si–C2–C9–C26	48.18	33.62	14.56	42.08	36.23	5.85	43.98
Si–C5–C6–C31	48.28	33.65	14.63	–2.00	–0.95	1.05	0.72
C2–C3–C8–C17	57.04	50.72	6.32	60.83	52.80	8.03	58.57
C5–C4–C7–C16	56.97	50.95	6.02	87.36	90.59	3.23	79.70
C5–Si–C10–C32	–23.72	–22.06	1.66	33.00	32.02	0.98	27.86
C2–Si–C11–C41	–24.29	–21.60	2.69	–69.37	–69.04	0.33	–69.37

^aReference 31.**Table 2.** Calculated VEE, EDM, and the Assignment for S_1 of HPS in the Gas and Solid Phases

S_1	VEE	expt	EDM	assignment
		Absorption		
gas phase ^a	3.10 eV (400 nm)	3.42 eV (363 nm)	4.20 D	HOMO → LUMO (95.7%)
solid phase ^b	3.07 eV (404 nm)	3.36 eV (369 nm)	5.29 D	HOMO → LUMO (98.2%)
		Emission		
gas phase ^a	2.22 eV (558 nm)	2.50 eV (497 nm)	5.20 D	HOMO → LUMO (98.1%)
solid phase ^b	2.32 eV (534 nm)	2.53 eV (490 nm)	5.85 D	HOMO → LUMO (98.4%)

^aIn cyclohexane solution, ref 21. ^bIn thin film, ref 59.

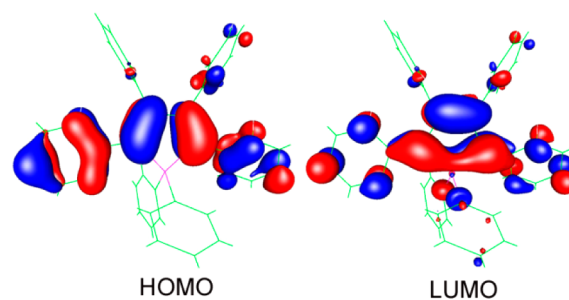
the latter issue, polarizable force fields (PFF) based on inducible point dipole,⁵⁵ fluctuating charge,⁵⁶ Drude oscillator,⁵⁷ and distributed multipoles⁵⁸ could be possible solutions. Both effects deserve further investigations.

III. RESULTS AND DISCUSSION

A. Geometric and Electronic Structures. We present the optimized structure of HPS at both S_0 and S_1 states in Table 1, together with the X-ray crystal structure for comparison.³¹ The predicted solid-phase structure at S_0 is in good agreement with the crystal structure, indicating the reliability of the adopted QM/MM approach. By analyzing the structural changes $|\Delta(S_0-S_1)|$ upon excitation, we can see that the torsional angles between the silacycle and two phenyl groups at the 2,5-positions (Si–C2–C9–C26 and Si–C5–C6–C31) show larger dihedral modifications (14.56° and 14.63°) in the gas phase than those (5.85° and 1.05°) in the solid phase, suggesting that the geometric relaxations of the phenyl rings at the 2,5-positions are largely hindered in the solid phase. Further, in the solid phase, we find the silacycle and the phenyl ring at the 5-position are almost coplanar, with the dihedral angle (Si–C5–C6–C31) of –2° at the S_0 minimum and –0.95° at the S_1 minimum, which remarkably increases the intramolecular conjugation. In addition, the torsional angles corresponding to the other four phenyls at the 1,1,3,4-positions (C2–Si–C11–C41, C5–Si–C10–C32, C2–C3–C8–C17, C5–C4–C7–C16) at the S_0 minimum are about 69°, 33°,

61°, and 87° in the solid phase, larger than those (24°, 24°, 57°, 57°) in the gas phase. Such twisted structures out of the silacycle plane effectively impede intermolecular π – π interaction through the central chromophore, and thus greatly prohibit excimer formation in the solid phase.

The calculated vertical excitation energies (VEE), electric transition dipole moment (EDM), and the assignment for S_1 are given in Table 2, together with the available experimental values. It can be seen that S_1 is dominated by the transition from the highest occupied molecular orbital (HOMO) to the lowest unoccupied molecular orbital (LUMO) in both gas and solid phases. The corresponding electronic density contours of HOMO and LUMO are plotted in Figure 2 and Figure S1 of

**Figure 2.** Electron density contours of HOMO and LUMO for the solid-phase HPS at the B3LYP/6-31G* level.

the Supporting Information, respectively. The HOMO is indicative of π character, and the LUMO demonstrates a conjugated $\sigma^*-\pi^*$ feature; i.e., the exocyclic C–Si bonds display σ^* character and the butadiene moiety shows π^* character. The electronic density of HPS is mainly distributed on the central silacycle and the neighboring phenyl groups at the 2,5-positions, and therefore the behaviors of these two phenyl rings are expected to dominate the optical properties. It can also be seen that, in the solid state, the molecular EDMs are larger (Table 2) and the HOMO–LUMO energy gap at the S_0 equilibrium geometry are smaller (Table S1, Supporting Information) than those in the gas phase. These stem from the increased intramolecular conjugation mentioned above.

We further calculated the rotational energy barriers by rotating the phenyl ring at the 2-position in the gas and solid phases (Figure 3, more details in Table S2, Supporting

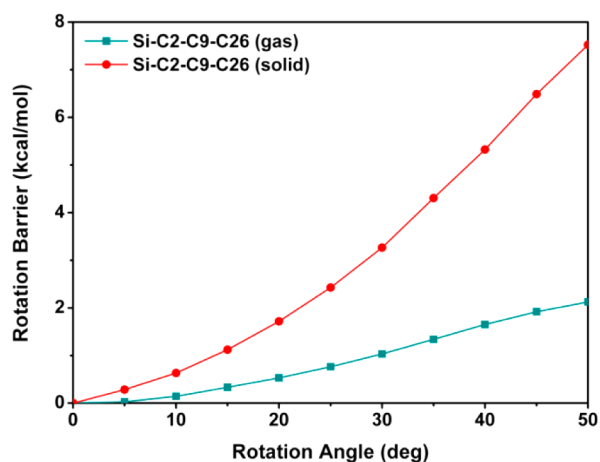


Figure 3. Rotational energy barrier obtained by rotating the dihedral angle (Si–C2–C9–C26).

Information). The rotational energy barrier is determined through the energy of the resulting geometry after rotation minus the energy of the equilibrium configuration. The rotation angle is expressed as the dihedral angle after rotation minus the dihedral angle at the equilibrium position. The resulting geometry after rotation is obtained by performing constrained optimization from each starting conformation with the changed dihedral. It is seen that the rotation energy barrier is much higher in the solid phase than in the gas phase, indicating this phenyl ring is more rigid and not susceptible to rotate in the solid phase, and therefore the 2-position restricted rotation results in the smaller structural changes $|\Delta(S_0-S_1)|$ in aggregates.

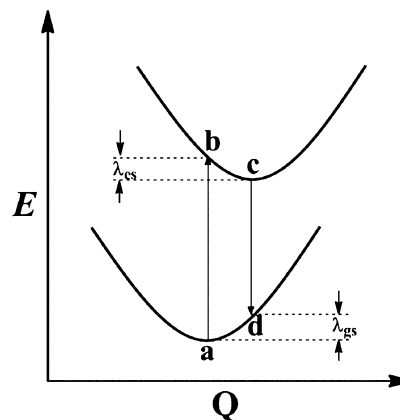
B. Huang–Rhys Factor and Reorganization Energy.

The reorganization energy from S_0 to S_1 and *vice versa* can be obtained by four-point calculations according to the adiabatic potential (AP) energy surface (Chart 2):

$$\begin{aligned}\lambda &= \lambda_{\text{gs}} + \lambda_{\text{es}} \\ \lambda_{\text{gs}} &= E(d) - E(a) \\ \lambda_{\text{es}} &= E(b) - E(c)\end{aligned}\quad (18)$$

where $E(a)$ is the total energy at the S_0 minimum, $E(b)$ is the total energy of S_1 at the S_0 equilibrium geometry, $E(c)$ is the total energy at the S_1 minimum, and $E(d)$ is the total energy of S_0 at the S_1 equilibrium geometry. The electronic energies (E)

Chart 2. Schematic Representation of the AP^a



^aQ refers to the nuclear configuration.

and zero-point vibrational energies (V) at a , b , c , d points, as well as the adiabatic excitation energies (ΔE_{ad}) in both the gas and solid phases are listed in Tables S3 and S4, Supporting Information. It can also be expressed as a summation of the contributions from normal mode (NM) relaxation in the harmonic oscillator approximation:

$$\begin{aligned}\lambda_{\text{gs}} &= \sum_{k \in \text{gs}} \lambda_k = \sum_{k \in \text{gs}} \hbar \omega_k HR_k \\ \lambda_{\text{es}} &= \sum_{k \in \text{es}} \lambda_k = \sum_{k \in \text{es}} \hbar \omega_k HR_k \\ HR_k &= \frac{\omega_k D_k^2}{2\hbar}\end{aligned}\quad (19)$$

where HR_k represents the Huang–Rhys factor for the k th mode and D_k is the displacement for the mode k between the equilibrium geometries of S_0 and S_1 . These quantities can be obtained by using DUSHIN program.^{39,41} The values of the reorganization energies obtained by AP and NM methods are very close (Table 3), indicating that the displaced harmonic oscillator approximation is quite reasonable in both gas and solid phases.

Table 3. Reorganization Energies λ Obtained by AP and NM Methods in Both Gas and Solid Phases

	gas phase		solid phase	
	AP	NM	AP	NM
λ_{gs} (meV)	407	420	379	402
λ_{es} (meV)	478	492	372	403

The HR factor and the reorganization energy of each normal mode are useful parameters measuring the extent of the electron–vibration coupling P_{kl} (eq 13). The HR factors for S_1 of HPS in the gas (solid) phase are depicted in Figure 4a (4b) and listed in Tables S5 (S6), Supporting Information. It can be seen that (i) HR factors of HPS are much smaller in the solid phase than in the gas phase, especially for the low-frequency region ($<200 \text{ cm}^{-1}$), suggesting that the low-frequency vibrations are hindered in the solid phase; (ii) modes with large HR factors (>0.6) all appear in the low-frequency region, e.g., modes 2 (26 cm^{-1}), 3 (31 cm^{-1}), 11 (65 cm^{-1}), 12 (66 cm^{-1}), 13 (77 cm^{-1}), 15 (96 cm^{-1}), 18 (142 cm^{-1}), and 20

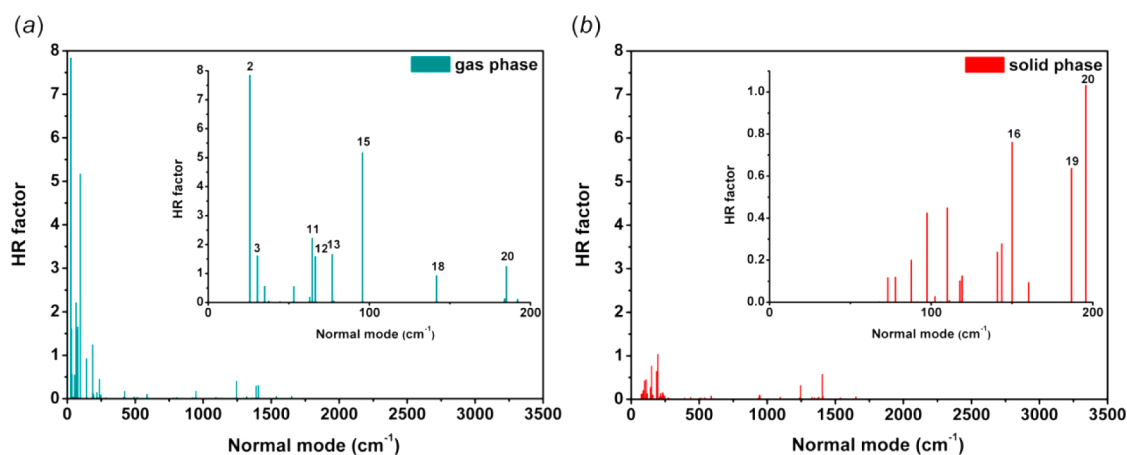


Figure 4. Calculated HR factors versus the normal-mode frequencies of single HPS molecule in the gas phase (a) and the solid phase (b). In each panel, the inset depicts the contributions from low-frequency range ($<200\text{ cm}^{-1}$) and labels the normal-mode sequences with large HR factors (>0.6).

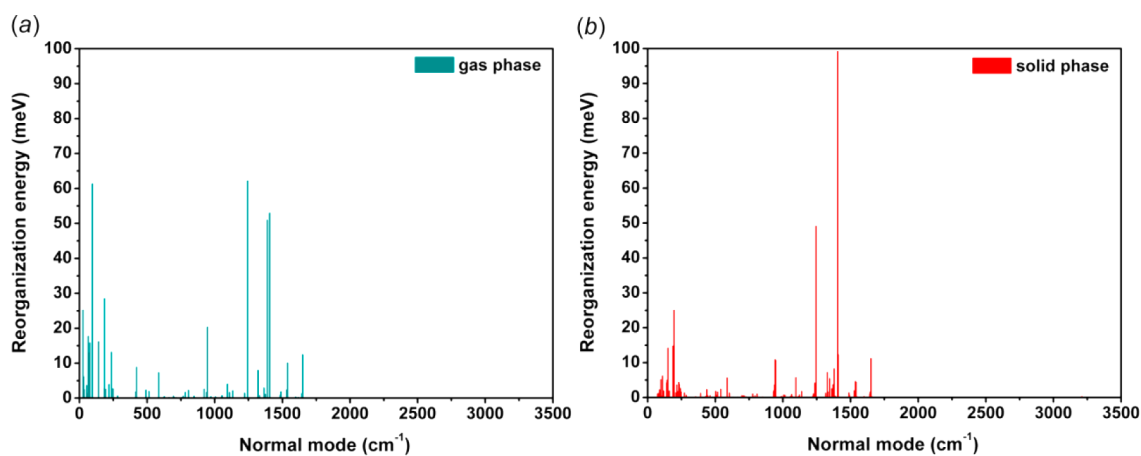


Figure 5. Calculated reorganization energies versus the normal-mode frequencies of HPS molecule in the gas phase (a) and the solid phase (b).

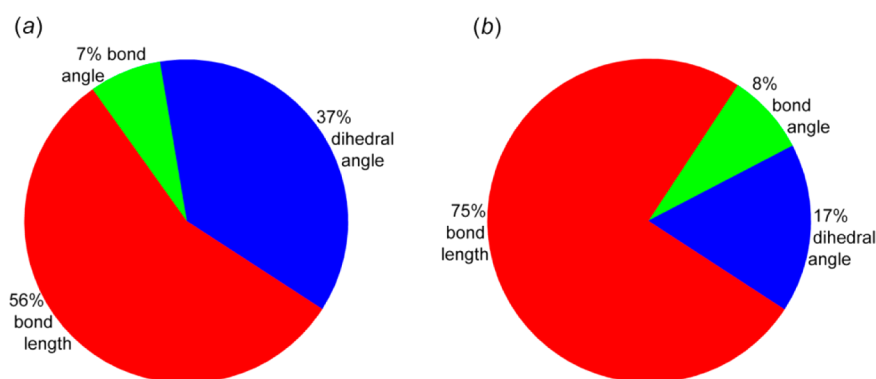


Figure 6. Contributions to the total reorganization energy from bond length, bond angle and dihedral angle of HPS in the gas phase (a) and the solid phase (b).

(185 cm^{-1}) in the gas phase and modes 16 (150 cm^{-1}), 19 (187 cm^{-1}), and 20 (196 cm^{-1}) in the solid phase. These modes are assigned as the twisting motions of the side phenyl rings from the normal mode displacement vectors, as shown in Figures S2 and S3, Supporting Information. It indicates the importance of low-frequency modes mixings in the excited-state nonradiative decay process.

We plot the reorganization energies for S_1 versus the normal-mode frequencies of HPS in both gas (Figure 5a) and solid

(Figure 5b) phases. We find: (i) The total reorganization energy is 492 meV in the gas phase, whereas it decreases to 403 meV in the solid phase. (ii) The contribution of all the low-frequency modes ($<200\text{ cm}^{-1}$) to the total reorganization energy is about 197 meV (40%) in the gas phase, whereas it is reduced to 84 meV (21%) in the solid phase. Thus, the decrease in the total reorganization energy mainly stems from the low-frequency modes upon aggregation. (iii) The contributions of high-frequency carbon–carbon stretching

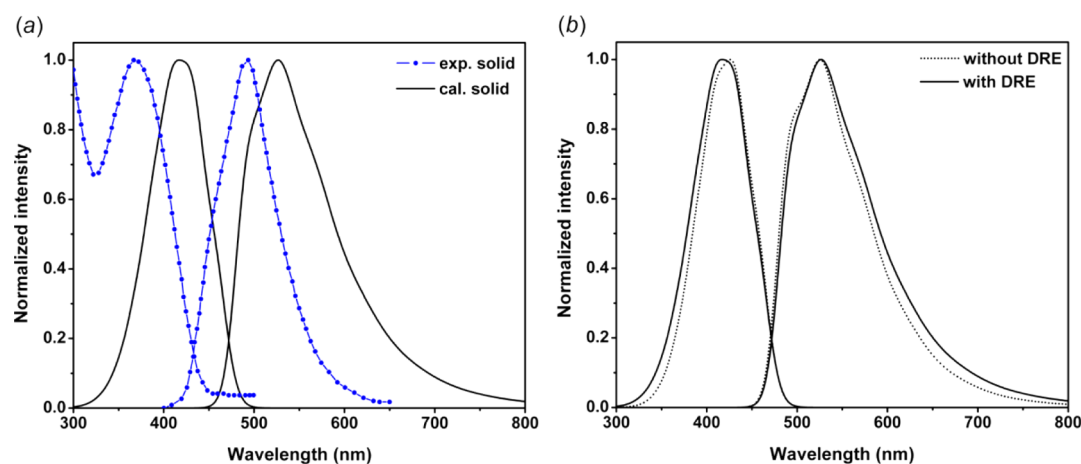


Figure 7. (a) Comparison of optical absorption and emission spectra between experiment (exp solid) and theory (cal solid) in the solid phase ($T = 300$ K). (b) Solid-phase spectra of HPS without DRE compared to those with DRE ($T = 300$ K).

vibration modes related to the central silacycle are large in both the gas and solid phases, as reflected by modes 137 (1243 cm^{-1}), 152 (1389 cm^{-1}), and 153 (1406 cm^{-1}) in the gas phase and modes 137 (1245 cm^{-1}), 152 (1405 cm^{-1}), and 153 (1409 cm^{-1}) in the solid phase (Figures S4 and S5, Supporting Information). Nevertheless, the summation of the reorganization energy over these three modes is 166 meV (34%) in the gas phase and 160 meV (40%) in the solid phase, implying that the high-frequency mode relaxation energies are insensitive to aggregation. These findings indicate that the energy dissipation pathways are easily quenched via low-frequency components upon aggregation. To clarify the relationship between the energy dissipation and the molecular structure, we project the reorganization energies in both the gas (Figure 6a) and solid (Figure 6b) phases onto the internal coordinate. Detailed internal coordinate representations (ICR) with reorganization energies larger than 1 meV are listed in Table S7, Supporting Information. It is noted that the contribution from the dihedral angles is 181 meV (37%) in the gas phase, but it is decreased to 68 meV (17%) in the solid phase. The main component is the dihedral angle associated with the phenyl-ring out-of-plane motions at the 2,5-positions, from 135 meV (27%) in the gas phase to 33 meV (8%) in the solid phase. These results further confirm the crucially important role of the phenyl-ring motions at the 2,5-positions in determining the photophysical properties, which is also fully consistent with the structure modification from S_0 to S_1 .

C. Solid-Phase Optical Spectra. The calculated vibrationally resolved solid-phase absorption and emission spectra of HPS at 300 K are shown in Figure 7a, including DRE. The calculated vibrational frequencies are scaled by a factor of 0.9614 .³⁹ We find that the theoretically predicted line shapes agree well with the experiments,⁵⁹ which again validate the TVCF approach and the QM/MM method adopted in this work. Both the absorption and emission maxima exhibit red shifts compared to the experimental results, and such underestimated excitation energies could be ascribed to the deficiency of hybrid functional.⁶⁰ For comparison, the calculated solid-phase spectra without considering DRE are also presented in Figure 7b. The spectra with DRE are slightly broader than those without DRE, which is in agreement with the conclusion drawn for ethylene.⁶¹ It is noticed that the distortion effect, namely, different frequencies at the S_0 and S_1 minima, leads to breakdown of the mirror-image symmetry

between absorption and emission.^{38,62} However, the calculated gas-phase spectra including DRE are much too broad. This problem might originate from the limitation of using the DRM to deal with flexible molecules such as HPS, where rotation and vibration degrees of freedom are strongly coupled. From this point, we may disentangle some modes with large rotation–vibration coupling from the fully mixing DRM, which deserves comprehensive investigation in the future.

D. Radiative and Nonradiative Decay Rates. The calculated k_r and k_{IC} are presented in Table 4. The following

Table 4. Calculated k_r and k_{IC} of Gas-Phase and Solid-Phase HPS ($T = 300\text{ K}$), “No DRE” Means without Considering DRE

300 K	k_r (s^{-1})		k_{IC} (s^{-1})	
	DRE	no DRE	DRE	no DRE
gas	1.05×10^7	4.76×10^7	3.76×10^{11}	6.65×10^5
solid	6.56×10^7	6.53×10^7	2.06×10^7	9.36×10^5

can be seen at 300 K : (i) DRE has no appreciable influence on k_r in both gas and solid phases, and such independence was also found in some previous gas-phase calculations concerning AIE-active APPEF²⁴ and DCDPP.²⁵ (ii) The radiative decay rate slightly increases from gas to solid state by about 6 times. This is mainly caused by the larger EDM, which is in turn controlled by the greater degree of intramolecular conjugation in the solid state. However, such a small increase in the radiative decay rate can hardly lead to so large an increase in the emission efficiency by forming aggregates. (iii) The inclusion of DRE reduces k_{IC} by about 4 orders of magnitude upon aggregation, and such a dramatic decrease results in an approximately 2000-fold increase in Φ_F [$\Phi_F = k_r/(k_r + k_{nr}) \approx k_r/(k_r + k_{IC})$], from 0.003% in the gas phase to 76% in the solid phase, in good agreement with the experimental AIE fact. If DRE is ignored, the IC rates are found to be kept almost unchanged from the gas to the solid phase, which contradicts the AIE fact. This finding again confirms that DRE is indispensable when the IC process for flexible molecules is considered. In fact, we find that this is closely related to remarkable reorganization energy: for some rigid phosphorescent molecules with small reorganization energy, the Duschinsky rotation does not play any appreciable role for both radiative and nonradiative decay rates.^{63,64} As explained before, the IC rate depends on the normal mode

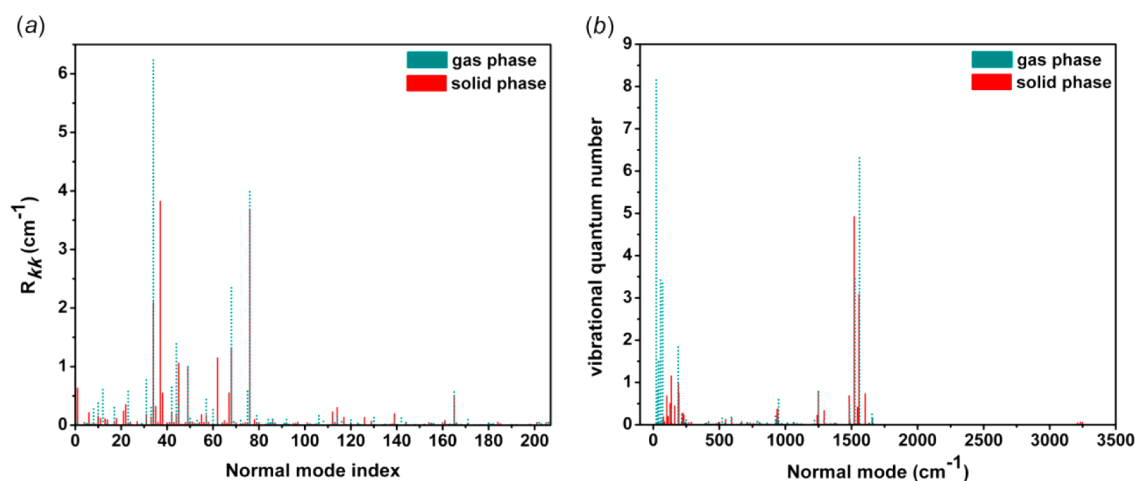


Figure 8. (a) Diagonal elements R_{kk} of the electronic coupling matrix R_{kl} versus the normal mode index of HPS in the gas (dotted columns) and solid (solid columns) phases. (b) Vibrational configuration of the final state related to the maximum IC rate under the “promoting mode” approximation for HPS in the gas (dotted columns) and solid (solid columns) phases.

overlap, which can only occur for the same mode if there is origin displacement. Once DRE is considered, the overlap can spread out to occur for different mode.²³ At room temperature, such a spread becomes much more pronounced than at low temperature. The predicted Φ_F considering DRE is underestimated in the gas phase compared to that in the experiment, indicative of the theoretically overestimated gas-phase k_{IC} . The disentanglement scheme toward the DRM may also bring about a reduced k_{IC} in the gas phase.

In addition to the nonradiative IC channels, other deactivation channels are also possible to dissipate the energy because the actual potential energy surfaces of the excited states are complex. Adachi et al. have noted that the ISC process would be fast (around 10^6 – 10^7 s^{-1}) when the energy gap between S_1 and T_1 levels is as small as 100 meV.^{65,66} We further mapped the potential energy surface of S_0 , T_1 , and S_1 along the dihedral angle (Si–C2–C9–C26) in both the gas phase (Figure S6a, Supporting Information) and the solid phase (Figure S6b, Supporting Information) at the B3LYP/6-31G* level. The conformation of each point with interval of 10° is determined through constrained optimization by freezing the dihedral angle (Si–C2–C9–C26) using DFT method. The energies of T_1 and S_1 were obtained by single-point vertical excitation-energy calculations using the TD-DFT approach. We find that the energy gap between S_1 and T_1 levels is considerably large (more than 1 eV). In addition, we calculated the SOC constant between S_1 and T_1 at the B3LYP/6-31G* level using two-component relativistic TD-DFT method implemented in the Beijing Density Functional (BDF) program.⁶⁷ The gas-phase and solid-phase SOC constants are obtained as 0.14 and 0.17 cm^{-1} , respectively. The large energy gaps and small SOC constants in both the gas and solid phases indicate that the rather slow ISC process is negligible compared to the radiative decay. The IC process is supposed to dominate the excited-state nonradiative decay and play the role as an “on–off” light emission switch. The main conclusion could be drawn that aggregation turns “on” the light emission by deactivating the nonradiative energy dissipation channel, which echoes the synergetic inhibition induced by 2-position restricted rotation and 5-position conjugated coplanarity.

To give more theoretical insights into the suppressed nonradiative channels in aggregates, we look at R_{kl} and P_{kl} in

eq 11. All the modes can contribute to k_{IC} through both diagonal and nondiagonal elements of the matrix R_{kl} instead of selecting one “promoting mode” in the conventional approach.^{23,26} We plot the diagonal part R_{kk} in Figure 8a, and the mode with the largest contribution is identified as the traditional “promoting mode”, i.e., mode 34 (409 cm^{-1}) in the gas phase and mode 37 (437 cm^{-1}) in the solid phase. It is seen that the summation of gas-phase R_{kk} over each normal mode is very close to the solid-phase one although there is slight difference in the distributions. Thus, it is P_{kl} sensitive to aggregation. The HR factor and reorganization energy of each normal mode associated with P_{kl} have been discussed in detail in section IIIB.

The vibrational quantum number contributed by each mode indicates the ability of that mode in the relaxation process. Therefore, we calculate the vibrational configuration ($T = 0$ K) of the final state when the IC rate reaches the maximum under the “promoting mode” approximation.³⁸ It is seen from Figure 8b that the vibrational quantum numbers contributed by the low-frequency modes (<200 cm^{-1}) (in the vicinity of 1) are largely decreased in the solid phase compared to those (about 1–8) in the gas phase. This directly illustrates that the nonradiative energy dissipation channel is suppressed via the low-frequency components in the solid phase.

IV. CONCLUSION

To summarize, the aggregation induced luminescent enhancement phenomenon of HPS was investigated by using the QM/MM approach coupled with the TVCF method. The theoretically predicted solid-phase optical spectra are in good agreement with the experiments. Our calculations show that (i) the motions of the phenyls attached to the central silacycle at the 2,5-positions are important in governing the photophysical properties, which are easily hindered in the solid phase via 2-position rotation restriction and 5-position coplanarity conjugation, (ii) HR factors, reorganization energies, and the vibrational quantum numbers in the solid phase become smaller compared to those in the gas phase, especially for the low-frequency modes, indicating the excited-state energy dissipation pathways are easily suppressed via low-frequency modes by aggregates formation, (iii) the inclusion of DRE well rationalizes the AIE fact; namely, at room temperature (300 K),

the nonradiative decay rate is predicted to be decreased by about 4 orders of magnitude upon aggregation, whereas the radiative decay rate only slightly increases. The excitonic effect as well as intermolecular charge delocalization deserves further consideration, which is in progress, in addition to the present elaborated study on intramolecular processes.⁶⁸

■ ASSOCIATED CONTENT

■ Supporting Information

Full author list of ref 54, supplementary figures containing gas-phase electron density contours, diagrammatic illustrations of selected normal modes, and potential energy surfaces, supplementary tables including HOMO and LUMO energies, rotation barriers at the 2-position, electronic and adiabatic excitation energies according to the AP, selected normal modes with large HR factors, selected ICR with large reorganization energy components, and the harmonic vibrational frequencies. This material is available free of charge via the Internet at <http://pubs.acs.org/>.

■ AUTHOR INFORMATION

Corresponding Authors

*Q. Peng. Tel: +86-10-82616830. E-mail: qpeng@iccas.ac.cn.

*Z. Shuai. Tel: +86-10-62797689. E-mail: zgshuai@tsinghua.edu.cn.

Notes

The authors declare no competing financial interest.

■ ACKNOWLEDGMENTS

T.Z. is deeply indebted to Dr. Likai Du and Dr. Qunyan Wu for the many helps about the ChemShell package. The authors thank Han Nie, Dr. Yuning Hong, and Prof. Zujin Zhao for valuable experimental discussions. Financial support from the National Natural Science Foundation of China (Grant Nos. 21290191, 91233105, and 91333202) and the Ministry of Science and Technology of China through the 973 program (Grant Nos. 2013CB834703, 2011CB932304, and 2013CB933503) are greatly acknowledged.

■ REFERENCES

- (1) Grimsdale, A. C.; Leok Chan, K.; Martin, R. E.; Jokisz, P. G.; Holmes, A. B. Synthesis of Light-Emitting Conjugated Polymers for Applications in Electroluminescent Devices. *Chem. Rev.* **2009**, *109*, 897–1091.
- (2) Yuan, W. Z.; Lu, P.; Chen, S. M.; Lam, J. W. Y.; Wang, Z. M.; Liu, Y.; Kwok, H. S.; Ma, Y. G.; Tang, B. Z. Changing the Behavior of Chromophores from Aggregation-Caused Quenching to Aggregation-Induced Emission: Development of Highly Efficient Light Emitters in the Solid State. *Adv. Mater.* **2010**, *22*, 2159–2163.
- (3) Jiang, T.; Jiang, Y. B.; Qin, W.; Chen, S. M.; Lu, Y. H.; Lam, J. W. Y.; He, B. R.; Lu, P.; Sung, H. H. Y.; Williams, I. D.; et al. Naphthalene-Substituted 2,3,4,5-Tetraphenylsiloles: Synthesis, Structure, Aggregation-Induced Emission and Efficient Electroluminescence. *J. Mater. Chem.* **2012**, *22*, 20266–20272.
- (4) Hong, Y. N.; Lam, J. W. Y.; Tang, B. Z. Aggregation-Induced Emission: Phenomenon, Mechanism and Applications. *Chem. Commun.* **2009**, 4332–4353.
- (5) Hong, Y. N.; Lam, J. W. Y.; Tang, B. Z. Aggregation-Induced Emission. *Chem. Soc. Rev.* **2011**, *40*, 5361–5388.
- (6) Wu, Q. Y.; Zhang, T.; Peng, Q.; Wang, D.; Shuai, Z. G. Aggregation Induced Blue-Shifted Emission – the Molecular Picture from a QM/MM Study. *Phys. Chem. Chem. Phys.* **2014**, *16*, 5545–5552.

(7) Chen, L.; Xu, S.; McBranch, D.; Whitten, D. Tuning the Properties of Conjugated Polyelectrolytes through Surfactant Complexation. *J. Am. Chem. Soc.* **2000**, *122*, 9302–9303.

(8) Taylor, P. N.; O'Connell, M. J.; McNeill, L. A.; Hall, M. J.; Aplin, R. T.; Anderson, H. L. Insulated Molecular Wires: Synthesis of Conjugated Polyrotaxanes by Suzuki Coupling in Water. *Angew. Chem., Int. Ed.* **2000**, *39*, 3456–3460.

(9) Hecht, S.; Fréchet, J. M. J. Dendritic Encapsulation of Function: Applying Nature's Site Isolation Principle from Biomimetics to Materials Science. *Angew. Chem., Int. Ed.* **2001**, *40*, 74–91.

(10) Nguyen, B. T.; Gautrot, J. E.; Ji, C.; Brunner, P.-L.; Nguyen, M. T.; Zhu, X. X. Enhancing the Photoluminescence Intensity of Conjugated Polycationic Polymers by Using Quantum Dots as Antiaggregation Reagents. *Langmuir* **2006**, *22*, 4799–4803.

(11) Wang, J.; Zhao, Y. F.; Dou, C. D.; Sun, H.; Xu, P.; Ye, K. Q.; Zhang, J. Y.; Jiang, S. M.; Li, F.; Wang, Y. Alkyl and Dendron Substituted Quinacridones: Synthesis, Structures, and Luminescent Properties. *J. Phys. Chem. B* **2007**, *111*, 5082–5089.

(12) Luo, J. D.; Xie, Z. L.; Lam, J. W. Y.; Cheng, L.; Chen, H. Y.; Qiu, C. F.; Kwok, H. S.; Zhan, X. W.; Liu, Y. Q.; Zhu, D. B.; et al. Aggregation-Induced Emission of 1-Methyl-1,2,3,4,5-Pentaphenylsilole. *Chem. Commun.* **2001**, 1740–1741.

(13) Tang, B. Z.; Zhan, X. W.; Yu, G.; Lee, P. P. S.; Liu, Y. Q.; Zhu, D. B. Efficient Blue Emission from Siloles. *J. Mater. Chem.* **2001**, *11*, 2974–2978.

(14) Oelkrug, D.; Tompert, A.; Gierschner, J.; Egelhaaf, H.-J.; Hanack, M.; Hohloch, M.; Steinhuber, E. Tuning of Fluorescence in Films and Nanoparticles of Oligophenylenevinyls. *J. Phys. Chem. B* **1998**, *102*, 1902–1907.

(15) Gierschner, J.; Park, S. Y. Luminescent Distyrylbenzenes: Tailoring Molecular Structure and Crystalline Morphology. *J. Mater. Chem. C* **2013**, *1*, 5818–5832.

(16) Spano, F. C.; Silvestri, L. Multiple Mode Exciton-Vibrational Coupling in H-aggregates: Synergistic Enhancement of the Quantum Yield. *J. Chem. Phys.* **2010**, *132*, 094704.

(17) Zhou, J.; Chang, Z. F.; Jiang, Y. B.; He, B. R.; Du, M.; Lu, P.; Hong, Y. N.; Kwok, H. S.; Qin, A. J.; Qiu, H. Y.; et al. From Tetraphenylethene to Tetranaphthylethene: Structural Evolution in AIE Luminogen Continues. *Chem. Commun.* **2013**, *49*, 2491–2493.

(18) Sonoda, Y.; Tsuzuki, S.; Goto, M.; Tohna, N.; Yoshida, M. Fluorescence Spectroscopic Properties of Nitro-Substituted Diphenylpolyenes: Effects of Intramolecular Planarization and Intermolecular Interactions in Crystals. *J. Phys. Chem. A* **2010**, *114*, 172–182.

(19) An, B.-K.; Kwon, S.-K.; Jung, S.-D.; Park, S. Y. Enhanced Emission and Its Switching in Fluorescent Organic Nanoparticles. *J. Am. Chem. Soc.* **2002**, *124*, 14410–14415.

(20) Liu, Y.; Tao, X. T.; Wang, F. Z.; Shi, J. H.; Sun, J. L.; Yu, W. T.; Ren, Y.; Zou, D. C.; Jiang, M. H. Intermolecular Hydrogen Bonds Induce Highly Emissive Excimers: Enhancement of Solid-state Luminescence. *J. Phys. Chem. C* **2007**, *111*, 6544–6549.

(21) Yu, G.; Yin, S. W.; Liu, Y. Q.; Chen, J. S.; Xu, X. J.; Sun, X. B.; Ma, D. G.; Zhan, X. W.; Peng, Q.; Shuai, Z. G.; et al. Structures, Electronic States, Photoluminescence, and Carrier Transport Properties of 1,1-Disubstituted 2,3,4,5-Tetraphenylsiloles. *J. Am. Chem. Soc.* **2005**, *127*, 6335–6346.

(22) Shuai, Z. G.; Peng, Q. Excited States Structure and Processes: Understanding Organic Light-Emitting Diodes at the Molecular Level. *Phys. Rep.* **2014**, *537*, 123–156.

(23) Peng, Q.; Yi, Y. P.; Shuai, Z. G.; Shao, J. S. Toward Quantitative Prediction of Molecular Fluorescence Quantum Efficiency: Role of Duschinsky Rotation. *J. Am. Chem. Soc.* **2007**, *129*, 9333–9339.

(24) Peng, Q.; Niu, Y. L.; Deng, C. M.; Shuai, Z. G. Vibration Correlation Function Formalism of Radiative and Non-Radiative Rates for Complex Molecules. *Chem. Phys.* **2010**, *370*, 215–222.

(25) Deng, C. M.; Niu, Y. L.; Peng, Q.; Qin, A. J.; Shuai, Z. G.; Tang, B. Z. Theoretical Study of Radiative and Non-Radiative Decay Processes in Pyrazine Derivatives. *J. Chem. Phys.* **2011**, *135*, 014304.

- (26) Li, M.-C.; Hayashi, M.; Lin, S.-H. Quantum Chemistry Study on Internal Conversion of Diphenyldibenzofulvene in Solid Phase. *J. Phys. Chem. A* **2011**, *115*, 14531–14538.
- (27) Wu, Q. Y.; Deng, C. M.; Peng, Q.; Niu, Y. L.; Shuai, Z. G. Quantum Chemical Insights into the Aggregation Induced Emission Phenomena: A QM/MM Study for Pyrazine Derivatives. *J. Comput. Chem.* **2012**, *33*, 1862–1869.
- (28) Wu, Q. Y.; Peng, Q.; Niu, Y. L.; Gao, X.; Shuai, Z. G. Theoretical Insights into the Aggregation-Induced Emission by Hydrogen Bonding: A QM/MM Study. *J. Phys. Chem. A* **2012**, *116*, 3881–3888.
- (29) Gao, X.; Peng, Q.; Niu, Y. L.; Wang, D.; Shuai, Z. G. Theoretical Insight into the Aggregation Induced Emission Phenomena of Diphenyldibenzofulvene: A Nonadiabatic Molecular Dynamics Study. *Phys. Chem. Chem. Phys.* **2012**, *14*, 14207–14216.
- (30) Li, Q. S.; Blancfort, L. A Conical Intersection Model to Explain Aggregation Induced Emission in Diphenyl Dibenzofulvene. *Chem. Commun.* **2013**, *49*, 5966–5968.
- (31) Chen, J. W.; Law, C. C. W.; Lam, J. W. Y.; Dong, Y. P.; Lo, S. M. F.; Williams, I. D.; Zhu, D. B.; Tang, B. Z. Synthesis, Light Emission, Nanoaggregation, and Restricted Intramolecular Rotation of 1,1-Substituted 2,3,4,5-Tetraphenylsiloles. *Chem. Mater.* **2003**, *15*, 1535–1546.
- (32) Wu, Q. Y.; Peng, Q.; Zhang, T.; Shuai, Z. G. Theoretical Study on the Aggregation Induced Emission. *Scientia Sinica Chimica* **2013**, *43*, 1078–1089.
- (33) Meyer, H.-D.; Miller, W. H. Analysis and Extension of Some Recently Proposed Classical Models for Electronic Degrees of Freedom. *J. Chem. Phys.* **1980**, *72*, 2272–2281.
- (34) Subotnik, J. E. Augmented Ehrenfest Dynamics Yields a Rate for Surface Hopping. *J. Chem. Phys.* **2010**, *132*, 134112.
- (35) Tully, J. C. Molecular Dynamics with Electronic Transitions. *J. Chem. Phys.* **1990**, *93*, 1061–1071.
- (36) Hammes-Schiffer, S.; Tully, J. C. Proton Transfer in Solution: Molecular Dynamics with Quantum Transitions. *J. Chem. Phys.* **1994**, *101*, 4657–4667.
- (37) Schmidt, J. R.; Parandekar, P. V.; Tully, J. C. Mixed Quantum-Classical Equilibrium: Surface Hopping. *J. Chem. Phys.* **2008**, *129*, 044104.
- (38) Jiang, Y. Q.; Peng, Q.; Gao, X.; Shuai, Z. G.; Niu, Y. L.; Lin, S. H. Theoretical Design of Polythiylenevinylene Derivatives for Improvements of Light-Emitting and Photovoltaic Performances. *J. Mater. Chem.* **2012**, *22*, 4491–4501.
- (39) Niu, Y. L.; Peng, Q.; Deng, C. M.; Gao, X.; Shuai, Z. G. Theory of Excited State Decays and Optical Spectra: Application to Polyatomic Molecules. *J. Phys. Chem. A* **2010**, *114*, 7817–7831.
- (40) Peng, Q.; Yi, Y. P.; Shuai, Z. G.; Shao, J. S. Excited State Radiationless Decay Process with Duschinsky Rotation Effect: Formalism and Implementation. *J. Chem. Phys.* **2007**, *126*, 114302.
- (41) Reimers, J. R. A Practical Method for the Use of Curvilinear Coordinates in Calculations of Normal-Mode-Projected Displacements and Duschinsky Rotation Matrices for Large Molecules. *J. Chem. Phys.* **2001**, *115*, 9103–9109.
- (42) Lin, S.-H. Rate of Interconversion of Electronic and Vibrational Energy. *J. Chem. Phys.* **1966**, *44*, 3759–3767.
- (43) Sherwood, P.; de Vries, A. H.; Guest, M. F.; Schreckenbach, G.; Catlow, C. R. A.; French, S. A.; Sokol, A. A.; Bromley, S. T.; Thiel, W.; Turner, A. J.; et al. QUASI: A General Purpose Implementation of the QM/MM Approach and Its Application to Problems in Catalysis. *J. Mol. Struct.: THEOCHEM* **2003**, *632*, 1–28.
- (44) Ahlrichs, R.; Bär, M.; Häser, M.; Horn, H.; Kölmel, C. Electronic Structure Calculations on Workstation Computers: The Program System Turbomole. *Chem. Phys. Lett.* **1989**, *162*, 165–169.
- (45) TURBOMOLE V6.5, University of Karlsruhe and of the Forschungszentrum Karlsruhe GmbH, 1989–2007; TURBOMOLE GmbH, since 2007 (accessed May 23, 2013).
- (46) Smith, W.; Forester, T. R. DL_POLY_2.0: A General-Purpose Parallel Molecular Dynamics Simulation Package. *J. Mol. Graphics* **1996**, *14*, 136–141.
- (47) Wang, J. M.; Wolf, R. M.; Caldwell, J. W.; Kollman, P. A.; Case, D. A. Development and Testing of a General Amber Force Field. *J. Comput. Chem.* **2004**, *25*, 1157–1174.
- (48) Zheng, X. Y.; Geng, H.; Yi, Y. P.; Li, Q. K.; Jiang, Y. Q.; Wang, D.; Shuai, Z. G. Understanding Lattice Strain Controlled Charge Transport in Organic Semiconductors: A Computational Study. *Adv. Funct. Mater.* **2014**, DOI: 10.1002/adfm.201400261.
- (49) Bayly, C. I.; Cieplak, P.; Cornell, W.; Kollman, P. A. A Well-Behaved Electrostatic Potential Based Method Using Charge Restraints for Deriving Atomic Charges: the RESP Model. *J. Phys. Chem.* **1993**, *97*, 10269–10280.
- (50) Cornell, W. D.; Cieplak, P.; Bayly, C. I.; Kollman, P. A. Application of RESP Charges to Calculate Conformational Energies, Hydrogen Bond Energies, and Free Energies of Solvation. *J. Am. Chem. Soc.* **1993**, *115*, 9620–9631.
- (51) Bakowies, D.; Thiel, W. Hybrid Models for Combined Quantum Mechanical and Molecular Mechanical Approaches. *J. Phys. Chem.* **1996**, *100*, 10580–10594.
- (52) Becke, A. D. Density-Functional Thermochemistry. III. The Role of Exact Exchange. *J. Chem. Phys.* **1993**, *98*, 5648–5652.
- (53) Lee, C.; Yang, W. T.; Parr, R. G. Development of the Colle-Salvetti Correlation-Energy Formula into a Functional of the Electron Density. *Phys. Rev. B* **1988**, *37*, 785–789.
- (54) Frisch, M. J.; Trucks, G. W.; Schlegel, H. B.; Scuseria, G. E.; Robb, M. A.; Cheeseman, J. R.; Scalmani, G.; Barone, V.; Mennucci, B.; Petersson, G. A.; et al. *Gaussian 09*, Revision D.01; Gaussian, Inc.: Wallingford, CT, 2013.
- (55) Sala, J.; Guàrdia, E.; Masia, M. The Polarizable Point Dipoles Method with Electrostatic Damping: Implementation on a Model System. *J. Chem. Phys.* **2010**, *133*, 234101.
- (56) Patel, S.; Mackerell, A. D.; Brooks, C. L. CHARMM Fluctuating Charge Force Field for Proteins: II Protein/Solvent Properties from Molecular Dynamics Simulations Using a Nonadditive Electrostatic Model. *J. Comput. Chem.* **2004**, *25*, 1504–1514.
- (57) Lamoureux, G.; Roux, B. Modeling Induced Polarization with Classical Drude Oscillators: Theory and Molecular Dynamics Simulation Algorithm. *J. Chem. Phys.* **2003**, *119*, 3025–3039.
- (58) Ponder, J. W.; Wu, C. J.; Ren, P. Y.; Pande, V. S.; Chodera, J. D.; Schnieders, M. J.; Haque, I.; Mobley, D. L.; Lambrecht, D. S.; DiStasio, R. A.; et al. Current Status of the AMOEBA Polarizable Force Field. *J. Phys. Chem. B* **2010**, *114*, 2549–2564.
- (59) Zhan, X. W.; Risko, C.; Amy, F.; Chan, C.; Zhao, W.; Barlow, S.; Kahn, A.; Brédas, J.-L.; Marder, S. R. Electron Affinities of 1,1-Diaryl-2,3,4,5-Tetraphenylsiloles: Direct Measurements and Comparison with Experimental and Theoretical Estimates. *J. Am. Chem. Soc.* **2005**, *127*, 9021–9029.
- (60) Lange, A.; Herbert, J. M. Simple Methods To Reduce Charge-Transfer Contamination in Time-Dependent Density-Functional Calculations of Clusters and Liquids. *J. Chem. Theory Comput.* **2007**, *3*, 1680–1690.
- (61) Mebel, A. M.; Hayashi, M.; Liang, K. K.; Lin, S.-H. Ab Initio Calculations of Vibronic Spectra and Dynamics for Small Polyatomic Molecules: Role of Duschinsky Effect. *J. Phys. Chem. A* **1999**, *103*, 10674–10690.
- (62) Deng, C. M.; Niu, Y. L.; Peng, Q.; Shuai, Z. G. Electronic Structures and Spectroscopic Properties of Group-14 Metalloles MPh₃ (M=Si, Ge, Sn). *Acta Phys.-Chim. Sin.* **2010**, *26*, 1051–1058.
- (63) Shi, Q. H.; Peng, Q.; Sun, S. R.; Shuai, Z. G. Vibration Correlation Function Investigation on the Phosphorescence Quantum Efficiency and Spectrum for Blue Phosphorescent Ir(III) Complex. *Acta Chimica Sinica* **2013**, *71*, 884–891.
- (64) Peng, Q.; Niu, Y. L.; Shi, Q. H.; Gao, X.; Shuai, Z. G. Correlation Function Formalism for Triplet Excited State Decay: Combined Spin-Orbit and Non-adiabatic Couplings. *J. Chem. Theory Comput.* **2013**, *9*, 1132–1143.
- (65) Uoyama, H.; Goushi, K.; Shizu, K.; Nomura, H.; Adachi, C. Highly Efficient Organic Light-Emitting Diodes from Delayed Fluorescence. *Nature* **2012**, *492*, 234–238.

(66) Ishimatsu, R.; Matsunami, S.; Shizu, K.; Adachi, C.; Nakano, K.; Imato, T. Solvent Effect on Thermally Activated Delayed Fluorescence by 1,2,3,5-Tetrakis(carbazol-9-yl)-4,6-Dicyanobenzene. *J. Phys. Chem. A* **2013**, *117*, 5607–5612.

(67) Li, Z. D.; Xiao, Y. L.; Liu, W. J. On the Spin Separation of Algebraic Two-Component Relativistic Hamiltonians. *J. Chem. Phys.* **2012**, *137*, 154114.

(68) Shuai, Z. G.; Liu, W. J.; Liang, W. Z.; Shi, Q.; Chen, H. Theoretical Study of the Low-lying Electronic Excited States for Molecular Aggregates. *Sci. China: Chem.* **2013**, *56*, 1258–1262.